Performance of glass fiber antiscatter devices at mammographic energies

Rebecca Fahrig, James G. Mainprize, and Normand Robert
Department of Medical Biophysics, University of Toronto, and Research Division, Sunnybrook Health Science Centre, 2075 Bayview Avenue, Toronto, Ontario M4N 3M5, Canada

Arthur Rogers
Synergistic Detector Designs, 5055 Brandin Court, Fremont, California 94538

Martin J. Yaffe
Departments of Medical Biophysics and Radiology, University of Toronto and Research Division, Sunnybrook Health Science Centre, 2075 Bayview Avenue, Toronto, Ontario M4N 3M5, Canada

(Received 20 October 1993; accepted for publication 12 May 1994)

Using fiber optic manufacturing techniques, it is possible to produce a radiographic grid that discriminates against scattered radiation in two dimensions. Such grids consist of septa composed of glass with a high lead content; the interspace material is air, so that approximately 80% of the grid area is open. In this way, effective high ratio grids can be produced with relatively low Bucky factors. The performance of samples of such grid material is characterized in terms of both scatter rejection and dose efficiency for application in digital mammography in both slot–beam and area–beam geometry. For area beams, five- to tenfold improved scatter rejection relative to conventional grids was observed. In slot configurations, such grids could provide improved SNR/dose performance and more effective utilization of the heat loading capability of the x-ray source.

Key words: mammography, scatter, grids

I. INTRODUCTION

When scattered radiation originating from the patient is recorded in a radiographic image, both subject contrast and the signal-to-noise ratio (SNR) of details in the image are reduced. Typical mammographic scatter-to-primary ratios (S/P) at the image receptor range from 0.3 to 1.0 depending on the thickness of the breast and on the tube potential.[1] The presence of scatter can cause up to a 50% reduction in contrast, and up to a 55% reduction (for constant total light output from the screen) in SNR. It is therefore important both for conventional film-screen radiography and for digital imaging to minimize the scatter that reaches the image recording device.

Current antiscatter grids for mammography are one-dimensional arrays of lead lamellae, separated by a more radiolucent "interspace" material. Common spacer materials are fiber and wood, with typical grid ratios (height of lamella : interspace thickness) of 4:1 or 5:1. The presence of the grid, while reducing scattered radiation, also leads to considerable attenuation of primary radiation. To compensate for the loss of this primary radiation as well as that of the rejected scattered radiation (which, although not forming a useful image, does contribute to film darkening), a higher dose to the patient is required to maintain the optical density of the film at its optimum operating point. The increase in dose is related to the Bucky factor (ratio of the entrance exposure required with the grid to that required without the grid) and is generally in the range of a factor of 2 (thin breasts) to 3 (thicker breasts) for currently available mammographic grids.[1] Note that for screen-film mammography, even an ideal grid, i.e., one that transmits all of the primary and none of the scattered radiation, would have a Bucky factor of between 1.3 and 2 depending on the thickness of the breast.[1]

We have tested the performance of samples of a two-dimensional air-interspaced material for rejection of scattered radiation in radiography. Because of our interest in digital mammography, our measurements have been performed at relatively low energies (30 kVp) and for geometries appropriate to the mammographic imaging task. In addition, we have investigated grid performance for geometries specific to a scanned slot digital detector. A slot system has relatively good scatter characteristics due to the reduced area of the breast irradiated at any given time. There are, however, practical limits to how narrow the slot width can be made, since a narrow beam requires increased imaging time and can impose excessive heat loading requirements on the x-ray tube. If an air-interspaced grid is used with the detector, the beam width may be increased somewhat while maintaining good SNR, with only a small penalty in increased dose to the patient. The shorter imaging time reduces image artifacts due to patient motion, increases x-ray tube life, and improves patient comfort.

II. MATERIALS AND METHOD

A photograph of the surface of one of the grids investigated below is shown in Fig. 1. The two-dimensional grids are fabricated using optical fiber technology in the form of fiber optic faceplates where the glass of the cladding of each "fiber" has a high lead content and where the core is composed of air. The glass cladding has an equivalent lead density of 3.79 g/cm^2, with a linear attenuation coefficient of $\sim$325 cm^{-1} at 20 keV and varies in wall thickness from 1.3–2.5 μm. The faceplate samples tested below are 2.5$\times$2.5 cm square. Table I summarizes the properties of the four fiber optic grids, and those of a commercial one-dimensional grid currently in use with the Transworld MAM II-C (now Continental X-ray Corp.) system for the purposes of comparison.

The grids were characterized in terms of four parameters.

 0094-2405/94/21(8)/1277/6/$1.20

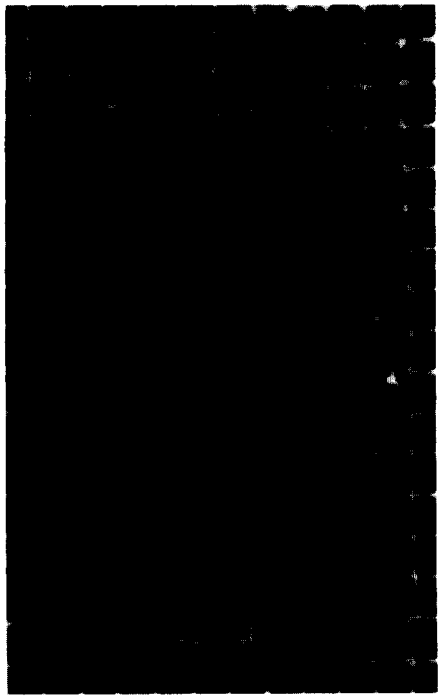

FIG. 1. Light image of fiber optic grid #1. The white line corresponds to approximately 0.5 mm on the image.

The primary and scatter transmission factors, T_p and T_s, respectively, are given by

$$T_p=\frac{P_g}{P} \quad \text{and} \quad T_s=\frac{S_g}{S},$$

where P_g and S_g are the primary and scattered radiation passing through the grid when the incident values are P and S.[2] The selectivity, Sel, is the ratio of T_P to T_S. For an ideal grid, T_p would be 1.0, T_s would 0, and the selectivity would be infinitely large. The Bucky factor (Bf), given by

$$\text{Bf}=\frac{P+S}{PT_p+ST_s},$$

describes the increase in exposure to the patient required to achieve the same optical density on a film when the grid is added to the system. Given these data, other parameters such as the scatter degradation factor $(1/(1+S/P))$ and the contrast improvement factor $(\text{Bf}\times T_p)$ can be calculated.

Measurements of S/P were performed using the geometry shown in Fig. 2. The system consists of an adjustable fore-collimator mounted on a tungsten anode x-ray tube. X rays from the tube impinge on the phantom and the resulting transmitted primary and scattered x rays then interact in a BGO scintillating crystal. Light from the crystal passes through a light pipe to a photomultiplier tube (PMT) (Hamamatsu RSN679) and the charge signal is integrated using an electrometer (Keithley 356 17EBS digital programmable dosimeter). Dark signal from the PMT is subtracted from each measured signal. Lead blockers are mounted at the surface of the phantom on thin sheets of polyester (30 μm), and the detector is placed 67 cm from the focal spot of the x-ray tube. Note that since the BGO crystal absorbs most of the x rays incident on it, the measurements quoted below represent *energy fluence* S/P as opposed to the *luminance*[3] S/P. The luminance S/P is measured using a clinical scintillating screen, and includes the effect of the different interaction efficiencies of the screen for scattered and primary radiation. Since the S/P is relatively insensitive to x-ray energy, knowledge of the interaction efficiency of primary and scattered radiation for a screen and of the spectral distribution incident on the screen, combined with the energy fluence S/P measured here, can, if desired, be used to predict the light output from the screen for the geometries in which our measurements were performed.

TABLE I. Summary of grid characteristics.

	Height (mm)	Lamellae thickness (μm)	Interspace thickness (μm)	Interspace material	% open area	grid ratio
Grid 1	2.00	19–25	170×180	Air	80.5	11.8:1
Grid 2	2.00	12.5–14	106×118	Air	80.8	17.8:1
Grid 3	3.23	19–25	170×180	Air	80.5	18.5:1
Grid 4	1.25	12.5–14	106×118	Air	80.8	11.2:1
Commercial	1.06	94	212	Fiber	69.3	5:1

The phantom is a 30×33-cm block of breast equivalent material (BR12), 5 cm thick. In order to simulate a more realistic scatter volume for mammography, the field size was restricted to 16×16 cm at the detector plane for the area measurements and to 16×0.93 cm for the slot measurements. All data were acquired with a tungsten target tube using a 30-kVp beam with an equivalent inherent filtration of 1 mm aluminum. The mean energy of the beam before filtration by the phantom was approximately 21.5 keV. The x-ray exposures were reproducible to within 0.5% and the tube kVp was stable to within ±0.1 kVp.

For the slot and fiber optic grid measurements, the detector consists of a 1.6-mm-diam pinhole in 1 mm of lead with a partially beveled edge, directly in contact with the 3.4-mm-thick BGO crystal [Fig. 2(b)]. In view of the wider angular distribution resulting from full area irradiation, a second, large pinhole (2.3-mm diameter in 0.6 mm of lead), also with a beveled edge, was used to measure the S/P for the area geometry and for the commercial grid. The angular response of the detector with respect to its central axis (θ=0) is shown in Fig. 3 for the large pinhole. At 61° from the normal to the detector surface, the response has dropped down to 25% of the peak value. The angular response for the smaller pinhole geometry is similar. The drop in sensitivity as a function of angle, for both pinhole geometries, is due to three effects: (1) the effective area of the detector drops as the angle increases, (2) the probability that light will not successfully propagate through the light pipe to the PMT increases, as the x-ray photon interaction occurs closer to the edge of the BGO, and (3) the probability of an x-ray photon cutting through the corner of the BGO material and not being detected also increases as the angle increases.

For the large pinhole, the half-angle for cutoff of the detector may be estimated from Fig. 3 to be 78°. For the small pinhole, cutoff occurs at approximately 72°. Although these apertures do not cover the full 90° field of scatter, calcula-

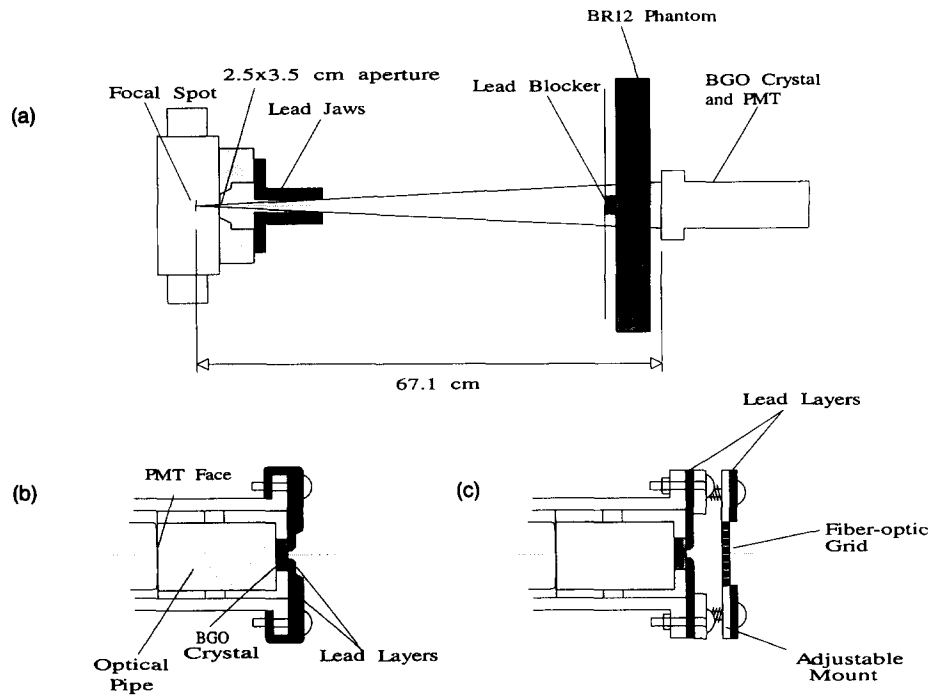

FIG. 2. (a) Experimental geometry used for measurements of S/P, including placement of lead blocker and lead collimator jaws. (b) Detail of x-ray detector, showing pinhole, BGO crystal, optical pipe, and PMT. (c) Detail of x-ray detector with adjustable grid mount in place.

tions by Chan and Doi[4] have shown that approximately only 2.5%–5% of the scatter exits the phantom at half-angles greater than 72°, and 1%–2% of the scatter exits the phantom at half-angles greater than 78°, depending on the energy of the incident photon. Large field S/P measurements are therefore underestimated by at most 4%, averaged over the energies in the spectrum. Error for the grid measurements at negligible, since the radiation is highly forward peaked after passing through the grid.

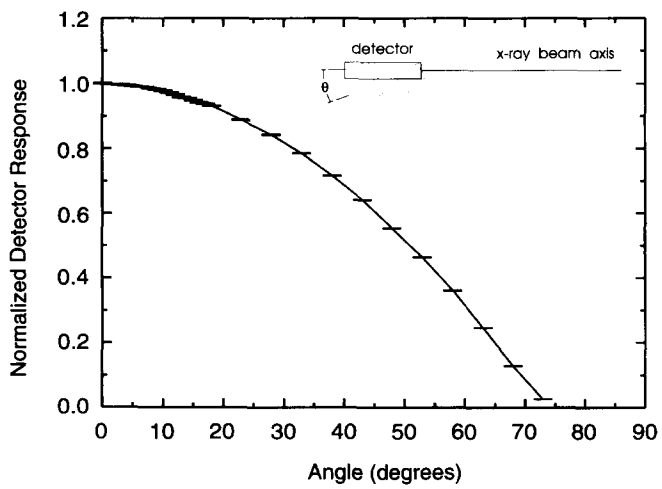

FIG. 3. Detector response vs angle θ, normalized to the response at $\theta=0$, for the large area/large pinhole geometry. Inset shows rotation of the detector about a point on the front face of the BGO crystal. Error bars in this figure and in all following figures represent one standard error.

The protocol followed is that first described by Yaffe *et al.*[5] for precise measurement of scatter and includes a correction for off-focal radiation. The scatter-to-primary ratio was measured for five blocker diameters, and extrapolation to zero blocker size was performed. Extrapolation is necessary in order to correct for the underestimation of the scatter that would have been created by primary quanta in the shadow of the blocker. For each blocker, four measurements were taken: M1, the signal, P_u+O_u, due to unattenuated primary and unattenuated off-focal radiation (no blocker, no phantom); M2, the signal, O_u (blocker only in the beam); M3, the signal, $S+O_a$, due to scattering in the phantom, and due to the attenuated off-focal radiation (blocker and phantom in the beam); and M4, the signal, $S+P+O_a$, due to scatter, primary, and attenuated off-focal radiation (phantom only in the beam). Using measurements M1, M3, and M4, the off-focal contribution to the signal behind the phantom was estimated as follows:

$$O_a(\text{est}) = \text{M2}\left[\frac{\text{M4}-\text{M3}}{\text{M1}-\text{M2}}\right],$$

and therefore S/P is given by

$$\text{S/P} = \frac{\text{M3}-O_a(\text{est})}{\text{M4}-\text{M3}}.$$

In the measurements which follow, the effect of the off-focal correction on S/P ranged from approximately 0.6%, for the area measurement with no grid, to 60% for the slot measurements with the fiber optic grid in place.

The grids were mounted directly on the surface of the scintillation detector as shown in Fig. 2(c). In order to ensure

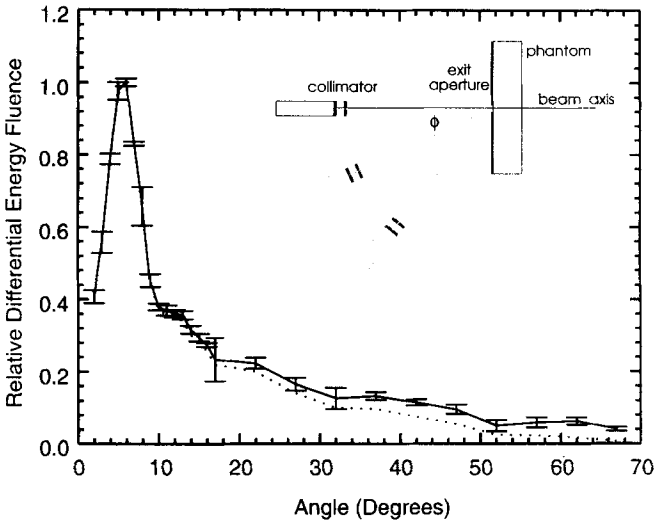

FIG. 4. Solid line: Measured relative differential energy fluence (normalized to the peak value) vs exit angle ϕ for the area geometry. Inset shows the measurement geometry. Dotted line: Corrected distribution detected during S/P measurements, for the same geometry, calculated by applying the correction for detector response (shown in Fig. 3 for the larger pinhole), as a function of angle.

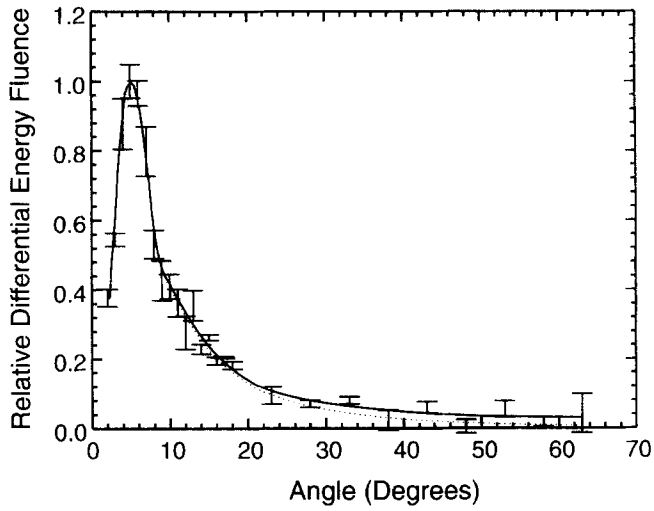

FIG. 5. Solid line: Measured relative differential energy fluence (normalized to the peak value) vs exit angle measured in the plane perpendicular to the direction of the collimating slot. Dotted line: Corrected distribution detected during S/P measurements, for the same geometry, calculated by applying the correction for detector response for the small pinhole.

that the axes of the grids were aligned on the central axis of the x-ray tube, three adjustment screws allowed fine adjustment of the angle of the grid mount, allowing the detector signal to be maximized. This alignment is particularly important since the fiber optic grids are not focused, and cutoff of primary radiation due to tilt would be significant. Note that alignment of the blockers and of the PMT on the central axis of the x-ray tube is also critical, so that primary radiation does not reach the detector during measurements M2 and M3.

III. RESULTS

In order to correct for the drop in detector sensitivity as a function of angle, the angular distribution of the radiation exiting from the phantom was measured in two geometries (slot and area), using the technique described by Muntz *et al.*[6] The BGO detector and a collimated aperture are swung in an arc centered on an aperture at the exit surface of the phantom, as shown in Fig. 4 (inset). The measured data are directly proportional to the differential scattering fluence, in units of energy per steradian per unit surface area with an angular resolution of approximately $\pm 1.0°$. Data for the area geometry are shown in Fig. 4, and the distribution in a direction perpendicular to the direction of the slot is shown in Fig. 5. Note that the peak angle of scatter for both geometries occurs at approximately 6°, in good agreement with the 3°–8° range for lucite, polyethylene, and water measured by Muntz *et al.*[6] As expected, a comparison of Figs. 4 and 5 shows that the scatter drops off faster as a function of angle for the slot geometry than for the area geometry.

The correction for detector sensitivity is performed by multiplying the angular distribution of the radiation by the angular response of the detector. This new distribution represents the scatter fluence seen by the detector during the S/P measurements, and is given by the dashed lines in Figs. 4 and 5. A ratio of areas before and after multiplication provides an estimate of the amount by which the measured S/P is an underestimate for the true values. For the area geometry without a grid in place, a correction of 13% was applied, while for the commercial grid, the correction was 1.2%. For the slot measurements without the fiber optic grids, in the direction perpendicular to the slot, the applied correction is 8%. In the direction parallel to the slot, the correction was taken to be equivalent to that for the area measurement without grid. We therefore applied an average correction to the slot data of 10.5%. For the fiber optic grid studies, the angular response of the detector (cutoff of the grid) with grid #1 in place, shown in Fig. 6, was such that correction was not necessary, since the response of the detector (i.e., without the grid in place) is virtually constant over the range of x-ray scatter angles incident on the detector. Note also that the

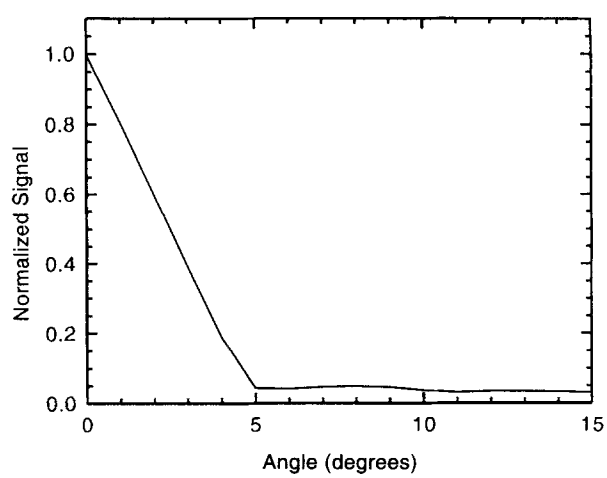

FIG. 6. Transmission vs incident angle of irradiation, for fiber optic grid #1.

TABLE II. Scatter characteristics of the grid samples in the large area geometry (5 cm BR-12 phantom, 16 ×16-cm field size at image receptor).

Geometry	S/P	T_P	T_S	Bf
Grid 1	$(7.39\pm0.07)\times10^{-3}$	0.789±0.004	$(1.04\pm0.01)\times10^{-2}$	1.967±0.009
Grid 2	$(6.50\pm0.08)\times10^{-3}$	0.801±0.004	$(9.3\pm0.1)\times10^{-3}$	1.94±0.01
Grid 3	$(1.32\pm0.07)\times10^{-3}$	0.776±0.003	$(1.82\pm0.09)\times10^{-3}$	2.011±0.009
Grid 4	$(2.38\pm0.01)\times10^{-2}$	0.797±0.003	$(3.37\pm0.02)\times10^{-2}$	1.915±0.008
Commercial	0.1040±0.0004	0.719±0.006	0.133±0.001	1.97±0.02
No grid	0.563±0.002	1	1	1

detector response with the grid in place falls to 25% at approximately 4°, which eliminates most of the low angle peak of the area scatter distribution, as well as the scatter from larger angles (see Fig. 4).

The S/P results for the four glass grids and for the commercial grid, measured in the large field geometry, are summarized in Table II. Note that although the density of lead in the lamellae is less for the fiber optic grids than it is for the conventional grid, the two-dimensional nature of the fiber optic grids and the increased thickness of the grids lead to improved scatter rejection. The S/P values measured with the fiber optic grids are 3–78 times lower than the S/P measured with the commercial grid, although the Bucky factors, or the increase in dose to the patient due to the use of the grid, are comparable.

The S/P results for the slot geometry are summarized in Table III. As expected, the scatter transmission values for the fiber optic grids increase in this geometry, since the incident scatter field is more forward peaked in the direction parallel to the slot due to the reduced area of irradiation. Primary transmission values remain the same within error. Note that for all four grids, the change from area to slot geometry results in a decrease in S/P by a factor of 2, while for the nongrid case, the same change results in a decrease in S/P by a factor of 4.5.

The estimate of error in the quoted measurements is due to statistical variation in x-ray production, interaction, and detection, and due to electrometer error. Another possible source of error that could lead to bias in the data (aside from the detector cutoff as discussed above) is alignment error. An estimate of maximum bias due to blocker positioning, or alignment, error leads to a possible deviation from the quoted values of at most 9%. This bias would generally lead to an overestimate of the S/P.

IV. DISCUSSION

The S/P measurement of 0.563 for the phantom alone (Table II) agrees well with published results given the differences in both geometry and phantom material. A value of 0.55 for the S/P from 4 cm of lucite may be extrapolated from the work of Barnes and Brezovich.[7] Since the density of lucite is slightly higher than that of tissue, 1.19 and ~1.0, respectively, a 4-cm thickness of lucite is equivalent to a 5-cm thickness of the breast equivalent material used for our measurements.[7] Their value agrees well with the S/P of 0.56 for 4 cm of polyethylene, measured by Fritz, Chang, and Livingston.[3] Monte Carlo studies by Dance *et al.*[8] also predict a value of 0.55 for a 5-cm-thick, 50% adipose–50% glandular breast. New data from Wagner[1] suggest a S/P for a 5-cm BR12 phantom of 0.76; however, exact details of the measurement technique and geometry are not available.

Since interspace material in the fiber optic grids is air, a further advantage of this particular design is the absence of scatter produced by x-ray interaction in the interspace. For a standard grid with aluminum or fiber interspace material, Dance and Day[9] estimate that this additional scatter leads to an increase in the S/P of approximately 0.03. The presence of this material may also lead to a small decrease in contrast in the image due to beam hardening effects.

The grids studied above are not focused. Therefore, if the grids were applied over a large area, cutoff of the primary would lead to severe degradation in grid performance. It is possible, however, to make focused glass fiber grids by applying the same technology used in manufacturing tapered fiber optic bundles.

Although it is challenging to apply the fiber optic grid technology to large-area moving grid systems, the application of this type of grid to a scanned slot digital system is

TABLE III. Scatter characteristics of the grid samples measured in the slot beam geometry.

Geometry	S/P	T_P	T_S	Bf
Grid 1	$(4.8\pm0.1)\times10^{-3}$	0.790±0.005	$(3.04\pm0.06)\times10^{-2}$	1.415±0.009
Grid 2	$(3.13\pm0.07)\times10^{-3}$	0.809±0.003	$(2.05\pm0.05)\times10^{-2}$	1.384±0.005
Grid 3	$(9.2\pm0.1)\times10^{-3}$	0.770±0.003	$(5.7\pm0.7)\times10^{-3}$	1.458±0.005
Grid 4	$(1.02\pm0.01)\times10^{-2}$	0.805±0.003	$(6.64\pm0.08)\times10^{-3}$	1.381±0.005
No grid	0.1234±0.0003	1	1	1

relatively easy. In such a system, the grid can be well supported along both edges of the slot, and could therefore be protected from breakage. In addition, as long as the area of the individual fibers is smaller than the pixel area by a factor of 2 or more, the grid lines would not be detected, and motion of the grid would not be required. Any fluctuations in detector pixel to pixel response due to presence of the grid could be corrected by using an appropriate flat-fielding technique which would be performed in any case for the digital detector.

V. CONCLUSIONS

We have characterized the behavior of four fiber optic grids for mammographic x-ray energies and for a phantom representing a typical breast thickness. Knowledge of the peak location of the scatter distribution provides important information for the design of effective scatter-rejection devices. The angular cutoff of the fiber optic grids eliminates a significant portion of the scatter distribution produced by the BR12 phantom. The grids display improved scatter rejection over that of a currently available commercial grid, and all of the grids studied here have approximately equal Bucky factors. Thus for the same increase in dose to the patient, the fiber optic grids can provide improved contrast.

[1]A. J. Wagner, "Contrast and grid performance in mammography," in *Screen Film Mammography Imaging Considerations and Medical Physics Responsibilities*, edited by G. T. Barnes and G. D. Frey (Medical Physics Publishing, Madison, WI, 1991), pp. 115–134.
[2]C. E. Dick and J. W. Motz, "New method for the experimental evaluation of x-ray grids," Med. Phys. **5**, 133–140 (1978).
[3]S. L. Fritz, C. H. J. Chang, and W. J. Livingston, "Scatter/primary ratios for x-ray spectra modified to enhance iodine contrast in screen-film mammography," Med. Phys. **10**, 866–870 (1983).
[4]H.-P. Chan and K. Doi, "Monte Carlo simulation in diagnostic radiology," in *Monte Carlo Simulation in the Radiological Sciences*, edited by R. L. Morin (CRC, Boca Raton, FL, 1988), p. 148.
[5]M. Yaffe, A. Fenster, and H. E. Johns, "Xenon ionization detectors for fan beam computed tomography scanners," JCAT **1**, 419–428 (1977).
[6]E. P. Muntz, T. Fewell, R. Jennings, and H. Bernstein, "On the significance of very small angle scattered radiation to radiographic imaging at low energies," Med. Phys. **10**, 819–823 (1983).
[7]G. T. Barnes and I. A. Brezovich, "The intensity of scattered radiation in mammography," Radiology **126**, 243–247 (1978).
[8]D. R. Dance, J. Persliden, and G. Alm Carlsson, "Calculation of dose and contrast for two mammographic grids," Phys. Med. Biol. **37**, 235–248 (1992).
[9]D. R. Dance and G. J. Day, "The computation of scatter in mammography by Monte Carlo methods," Phys. Med. Biol. **29**, 237–247 (1984).